



Originally published as:

Bindi, D., Zaccarelli, R., Strollo, A., Di Giacomo, G. (2019): Harmonized local magnitude attenuation function for Europe using the European Integrated Data Archive (EIDA). - *Geophysical Journal International*, 218, 1, pp. 519—533.

DOI: <http://doi.org/10.1093/gji/ggz178>

Harmonized local magnitude attenuation function for Europe using the European Integrated Data Archive (EIDA)

D. Bindi,¹ R. Zaccarelli,¹ A. Strollo¹ and D. Di Giacomo²

¹Helmholtz Centre Potsdam, GFZ German Research Centre for Geosciences, Telegrafenberg 14473, Potsdam, Germany. E-mail: bindi@gfz-potsdam.de

²International Seismological Centre ISC, Thatcham, Berkshire, RG19 4NS, UK

Accepted 2019 April 12. Received 2019 April 10; in original form 2019 January 24

SUMMARY

We derive a harmonized local magnitude scale across Europe using data disseminated by network operators through the European Integrated Data Archive (EIDA). We first calibrate simultaneously a set of non-parametric attenuation functions regionalized by considering six different regions covering central and southern Europe, anchoring the models to the Richter's scale at 17 km. Uncertainties on the attenuation coefficients, station corrections and magnitude values are evaluated through bootstrap analysis. The obtained attenuation functions show significant differences among the regions, up to 0.4 m.u. at 400 km, being the attenuation of the Wood–Anderson amplitude stronger for regions in the Mediterranean area. The non-parametric attenuation functions capture the changes in the rate of attenuation with distance due to the effects of later arrivals generated by crustal heterogeneity. A second calibration is performed to derive a parametric attenuation model. We consider a piece-wise linear function to describe the attenuation with the logarithm of distance, introducing two breakpoint distances at 10 and 60 km. For distances above 10 km, we also consider the anelastic attenuation term. We apply a mixed effect regression with network-dependent random effects on the anelastic coefficients. The parametric analysis confirms the stronger attenuation for networks operating in the Mediterranean area, such as the Italian and Greek networks, with respect to networks located in continental Europe. The network-dependent random effects allow us to quantify the between-network variability for different networks operating in the same region or country. The observed between-network variability is within ± 0.2 m.u., smaller than the variability among the six regions.

Key words: Earthquake ground motions; Earthquake source observations; Seismic attenuation.

1 INTRODUCTION

The local magnitude M_l introduced by Richter (1935) was the first quantitative measure of the earthquake size. Since M_l is routinely computed by seismological observatories to measure the size of local earthquakes, it often appears in empirical conversion relationships applied to create homogeneous magnitude catalogues for applications such as seismic hazard assessment (Grünthal & Wahlström 2012). Although M_l was introduced as an empirical parameter not representing any specific source characteristics, it has been shown to be connected to stress drop and rupture velocity (Deichmann 2017) and to scale with energy (Kanamori *et al.* 1993; Deichmann 2018). Therefore, M_l gained the interest of recent studies dealing with ground motion variability since it captures better than moment magnitude the high frequency ground shaking variability for moderate size earthquakes (Bindi *et al.* 2018, 2019a). Originally, the Richter magnitude was calibrated in southern California; when it is computed for networks deployed in regions with different attenuation characteristics, the attenuation function has to be recalibrated, selecting a reference distance to anchor the new attenuation model to the Richter one (Hutton & Boore 1987; Alsaker *et al.* 1991). In Europe, several magnitude scales have been calibrated in the past, considering networks with different extensions (Alsaker *et al.* 1991; Spallarossa *et al.* 2002; Stange 2006; Bindi *et al.* 2007; Booth 2007; Di Bona 2016; Scordilis *et al.* 2016; Kiliç *et al.* 2017; Chovanová & Kristek 2018; Luckett *et al.* 2018, among others). Comparisons among catalogues compiled by different observatories or agencies are not always straightforward due to differences in the procedure followed during the calibration of M_l . With the recent development of the European Integrated Data Archive (EIDA, <http://www.orfeus-eu.org/data/eida/>), an open-access infrastructure where data from different networks operating in Europe are archived and disseminated following common standards, we have the opportunity to derive an harmonized local magnitude scale by taking advantage of the dense and high quality data collected across Europe in recent years. The development of a

Table 1. Criteria applied to download segments for different European regions.

Area	Time span	Minimum magnitude	Longitude [min:max]	Latitude [min:max]
Continental Europe	01/1990-05/2018	2.5	[-12.0:26.5]	[45.5:71.0]
Iberia	01/1990-01/2018	2.5	[-12.0:8.0]	[34.0:45.45]
Italy	01/2010-07/2016	3.0	[8.05:19.0]	[36.5:45.45]
Italy	08/2016-03/2018	4.4	[8.05:19.0]	[36.5:45.45]
Italy	01/1990-12/2009	4.0	[8.05:19.0]	[36.5:45.45]
Greece–Turkey	01/1990-08/2018	3.5	[19.0:46.0]	[34.0:42.5]

local magnitude scale using a documented and modern technique for the European continent would generate several advantages such as the possibility to complement amplitude readings and unify catalogues from different seismic networks, particularly for earthquakes recorded among different networks. Moreover, it would facilitate the empirical conversions between local and moment magnitudes when creating seismic catalogues for hazard assessment purpose. Finally, it would allow to account for region-dependent features affecting the attenuation in different regions within Europe.

We first present the steps followed to compute the Wood–Anderson amplitudes (Uhrhammer & Collins 1990) by using a suite of programs developed to optimize, and easily customize, the download and processing of segments extracted from data repositories implementing the International Federation of Digital Seismograph Network standards (FDSN), such as EIDA or the Incorporated Research Institutions for Seismology (IRIS). Then, we present the calibration of a non-parametric local magnitude scale with regionalized attenuation functions, considering six different regions. Finally, a parametric attenuation model is derived by applying a mixed-effects approach with network-dependent attenuation adjustments.

2 DATA SET

To develop the local magnitude scale for Europe, we take advantage of EIDA for creating the necessary data set of waveforms and related metadata. EIDA is a federation of data centres which archive and disseminate waveform data and metadata gathered by numerous European research infrastructures, using standard FDSN services. To access, download and pre-processing the waveforms, we use *stream2segment* (Zaccarelli 2018; Zaccarelli *et al.* 2019), a Python package designed for helping the user in the whole workflow of downloading, inspecting and processing event-based seismic data. The steps followed in our analysis are described in the following sections.

2.1 Download from EIDA

The package *stream2segment* allows to create a relational data base (e.g. PostgreSQL or SQLite) where the segments extracted from the continuous data streams are stored along with their parametric information. In this study, the event catalogue used to guide the segment extraction is compiled using the event webservice of the European Mediterranean Seismological Centre (EMSC). The criteria for selecting the segments to be downloaded are defined in a configuration file that, among others, includes parameters related to spatial constraints adopted during download. An excerpt of the configuration file reporting such parameters is outlined in Table 1. For all regions listed in Table 1, stations are searched within a radius of 3° from the epicentres of events with magnitude smaller than 3.5, within a radius of 6° for magnitudes larger than 5.5, and a linear interpolation over the distances is applied for magnitudes in-between. Only events with depth shallower than 50 km and recorded by public accessible networks are considered in this study. From each stations, we downloaded segments 4 min long, starting 1 min before the theoretical first *P*-wave arrival time, requesting all available streams with a minimum sampling rate of 50 Hz. In the following, colocated instruments (e.g. strong motion and broad-band) are treated as different stations.

2.2 Processing

A processing pipeline is applied to segments stored in the local data base passing a first quality check (QC1) that consists in selecting segments without gaps or overlap and a percentage of missing data smaller than 50 per cent of the total requested amount. Segments with maximum amplitude exceeding a saturation threshold, set to 80 per cent of the expected maximum number of counts for the specific digitizer (Cauzzi *et al.* 2016), are also discarded. An a-causal Butterworth bandpass filter is applied, with high-pass corner selected according to the magnitude retrieved from the EMSC event-catalogue. The high-pass corner frequency (f_{HP}) is set to 0.4 Hz for magnitude $M \leq 4.5$, to 0.2 Hz for $4.5 < M \leq 5.5$, to 0.1 Hz for $5.5 < M \leq 6.5$ and to 0.05 Hz for $M > 6.5$. The low-pass frequency (f_{LP}) is set to 90 per cent of the Nyquist frequency. Before filtering, the linear trend is removed, signals are cosine-tapered at both ends and zero-padded (Converse & Brady 1992). The instrumental response is removed from the filtered waveforms. The presence of other events in the coda is checked by computing the normalized (and smoothed) second derivative of the cumulated squared acceleration and checking the presence of more than one peak above 0.9. The evaluation is performed over the time window corresponding to the 5–95 per cent of the total cumulated squared acceleration and waveforms showing a second peak after 10 s from the main peak are discarded. Finally, the synthetic Wood–Anderson trace is computed

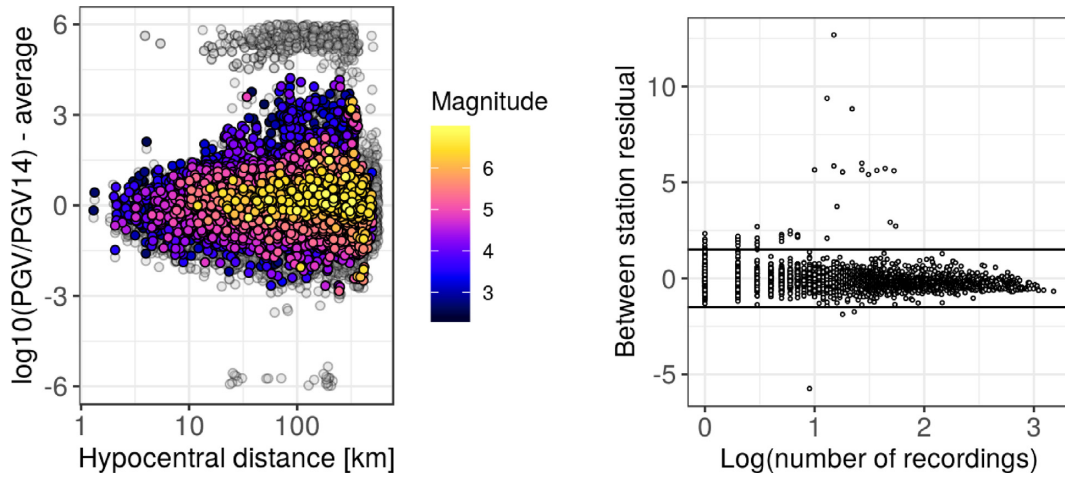


Figure 1. Left-hand panel: residuals for PGV with respect to Bindi *et al.* (2014). Symbols colour coded with EMSC magnitude indicate data selected for the analysis. Right-hand panel: between-station residuals $\delta S2S$ versus logarithm of the number of recordings, computed for PGV using the Bindi *et al.* (2014) GMPE.

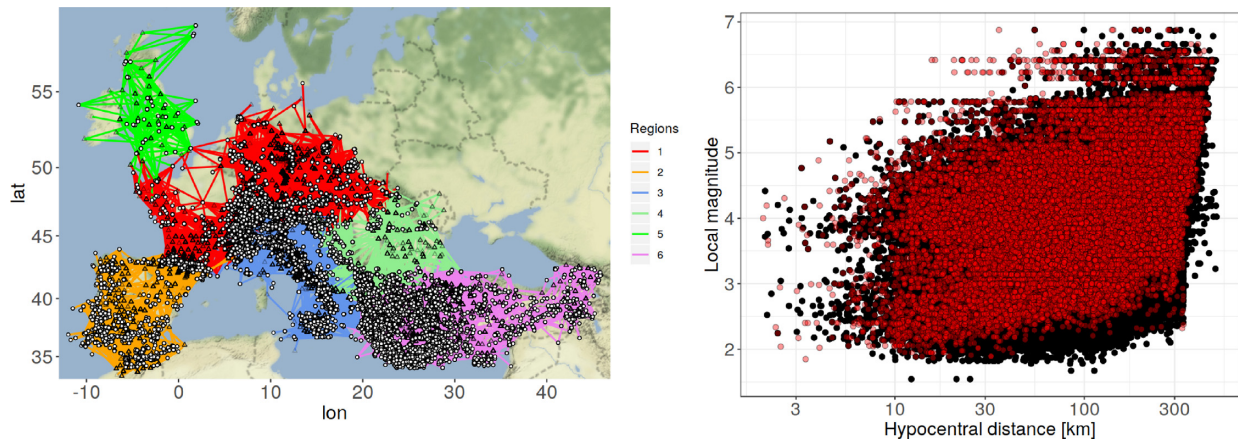


Figure 2. Left-hand panel: event (white circle) to station ray paths for the considered data set, colour coded according to the six considered regions. Right-hand panel: magnitude versus hypocentral distance scatterplot for the selected recording; red symbols indicate strong motion data, black symbols recordings from broad-band and short period sensors.

(considering a static magnification of 2080 and a natural period of 0.8 s), the maximum value evaluated and the geometrical mean of the values over the two horizontal components is considered for developing the local magnitude scale.

The second level of selection (QC2) is applied in two steps. The first step is based on the signal to noise ratio (SNR). The SNR is computed over four spectral windows: from f_{HP} to 1 Hz; from 1 to 10 Hz; from 10 to f_{LP} Hz; from f_{HP} to f_{LP} . We set the thresholds for the four spectral intervals to 2, 8, 2, 3, respectively. The thresholds were decided after preliminary tests and considering that the 1–10 Hz spectral interval is the most interesting for the analysis presented in this work. The second step is based on residual analysis with respect to predictions from two Ground Motion Prediction Equations (GMPEs) considering the peak ground velocity (PGV) and acceleration (PGA) (Bindi *et al.* 2014, 2017). In particular, the between-events δB and the station-to-station ($\delta S2S$) residuals (Al Atik *et al.* 2010; Kotha *et al.* 2017) are computed by grouping the observed minus predicted values either per earthquake or per station.

Fig. 1 exemplifies the PGV residuals for the selected recordings, considering one of the two GMPEs (Bindi *et al.* 2014). The distribution of the between-station $\delta S2S$ is shown as well. In the following, only stations s characterized by $|\delta S2S_s| < 1.5$ and events e corresponding to $|\delta B_e| < 1.5$ for both GMPEs and both intensity measures are further considered. Moreover, single recorded events and stations with only one record are also discarded. By applying our quality controls we intend to remove spurious measurements and large outliers in an efficient and practical way. As a result, from 428 000 segments passing QC1, the data set is reduced to 205 300 records from 12 721 earthquakes after applying QC2. Regarding the stations, 772 channels out of 2812 are from strong motion instruments.

3 NON-PARAMETRIC CALIBRATION

We calibrate a local magnitude scale following a non-parametric approach (Savage & Anderson 1995; Spallarossa *et al.* 2002; Bindi *et al.* 2018). In order to account for possible regional variation in the attenuation with distance, we introduce six regions as shown in Fig. 2 and

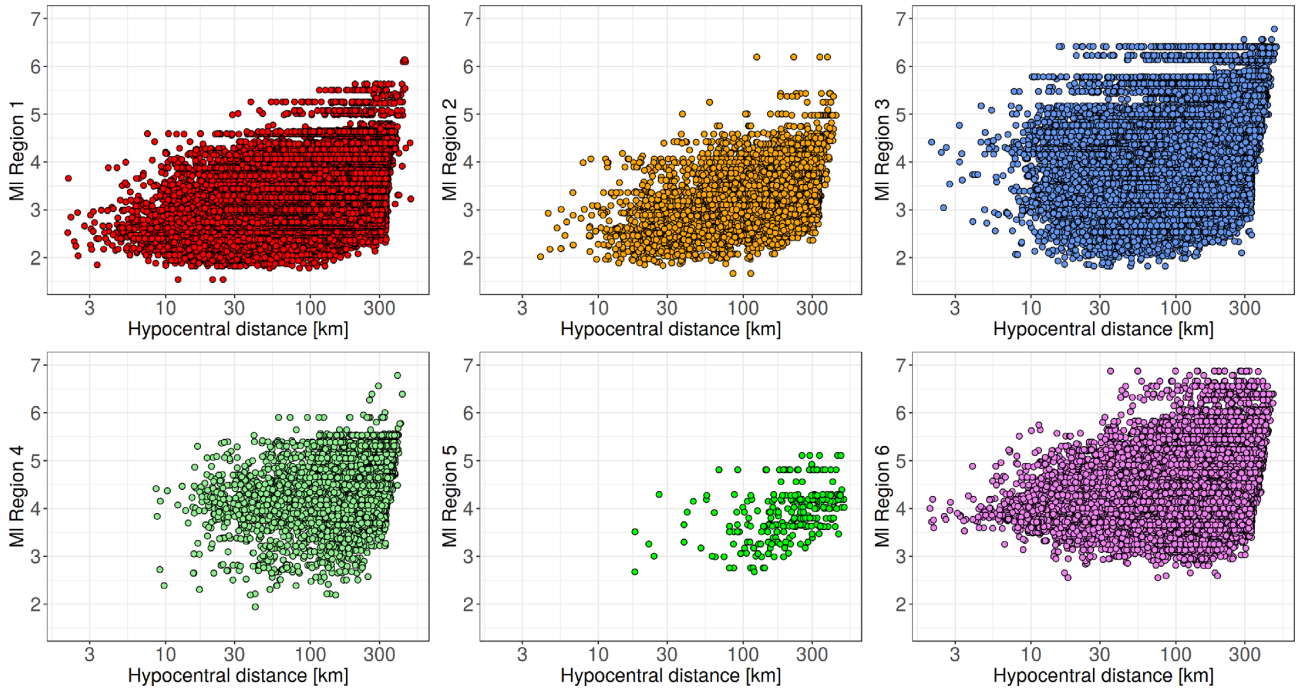


Figure 3. Scatterplot for six regions shown in the map of Fig. 2.

corresponding to Central Europe (Region 1), Iberia-Maghreb (Region 2), Central Mediterranean (Region 3), Balkans (Region 4), British Isles (Region 5) and Aegean-Anatolia (Region 6). Due to the small number of recordings in the selected data set, Scandinavia region is not considered in this study. The non-parametric model is described by

$$\log A_{kl}(R) = a_n \log A_0^{\text{region}}(R_n) + a_{n+1} \log A_0^{\text{region}}(R_{n+1}) + \sum_{i=1}^{N_{\text{event}}} MI_i \delta_{ik} + \sum_{j=1}^{N_{\text{station}}} S_j \delta_{jl}, \quad (1)$$

where $\log A_{kl}$ is the logarithm in base 10 of the Wood–Anderson amplitude (measured in mm) of event k recorded at station l . The three distance ranges from 1 to 100 km, from 100 to 200 km, and from 200 to 400 km are discretized in equal spaced bins 5, 10 and 20 km wide, respectively. In eq. (1), R_n , with $n = 1, \dots, 41$, are the nodes separating the distance bins and the hypocentral distance R is such that $R_n \leq R < R_{n+1}$; $a_n = (R_{n+1} - R)/\Delta R$; $\Delta R = (R_{n+1} - R_n)$; $a_{n+1} = 1 - a_n$; δ_{ik} and δ_{jl} are Kronecker deltas that allow the use of dummy variables; MI_i is the local magnitude of earthquake i ; S_j is the station correction of station j ; N_{station} and N_{event} are the number of station and earthquakes, respectively.

In eq. (1), a different non-parametric attenuation model $\log A_0^{\text{region}}$ is calibrated simultaneously for each region. The linear system is solved subject to the constraints that $\sum_j^{N_{\text{ref}}} S_j = 0$ and $\log A_0^{\text{region}}(17) = -2$ for all regions, where N_{ref} is a set of stations assumed as reference (i.e. the average of the logarithm of site corrections is constrained to zero). Following (Hutton & Boore 1987), we set the reference distance at 17 km to anchor the European magnitude scale to the California one near the source. Several preliminary calibrations were performed to select the most suitable reference site condition. The final choice was to use the average of the Italian seismic network (FDSN network code IV) as reference: since IV is a large seismological network contributing to several regions (i.e. regions 1, 3, 4 and 6) and it recorded a large number of earthquakes, its choice as reference led to the most stable inversion results. Moreover, we require the numerical second derivative of $\log A_0$ to be small. The linear system in eq. (1) is solved in least-squares sense (Koenker & Ng 2017) and uncertainties are estimated through bootstrap analysis (Efron 1979). The scatter plots of the magnitude–distance distribution used for the magnitude calibration are shown in Figs 2 and 3.

3.1 Non-parametric results

Fig. 4 shows the non-parametric attenuation curves obtained for the six considered regions. For each region, the results of 500 bootstrap replications are compared to the Hutton & Boore (1987) model for southern California (black curves). The bootstrap analysis shows that the data set allows to get stable results for all regions except for the British Isles, which requires additional data to constrain the regional attenuation. Differences in the attenuation among the regions are evident, the attenuation being strongest in region 6 and weakest in region 2, and reaching a difference of about 0.4 magnitude units (m.u.) at 400 km. Regions 1 and 2 show stronger attenuation than California in the first 60 km about; then, the attenuation curves flatten due to the effect of later arrivals, particular evident in region 1; for distances above 100–120 km, the attenuation rate in these two regions is similar to the California one. Regarding Region 5, the bootstrap attenuation curves

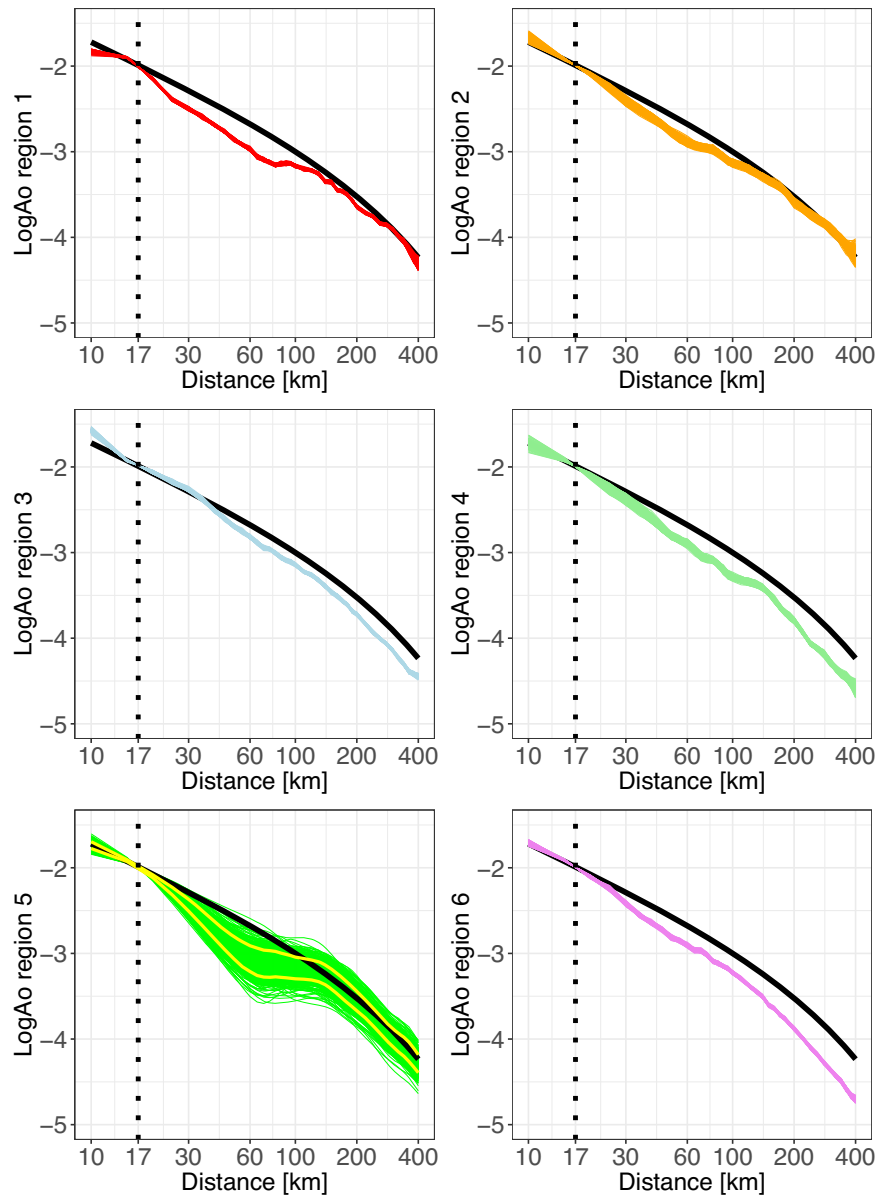


Figure 4. Non-parametric attenuation curves $\log A_0$ for different regions (see Fig. 2) obtained considering 500 bootstrap replications of the original data set. Black curve represents the model for southern California (Hutton & Boore 1987). For region 5, the yellow curves correspond to the 5th and 95th percentile of the bootstrap solutions.

show a larger dispersion than for the other regions since a much smaller data set is analysed (Fig. 3). Nevertheless, considering the 5th and 95th percentiles of the bootstrap distribution (yellow curves in Fig. 4), the trend of the attenuation with distance is similar to Region 1. The station corrections, grouped by network, are shown in Fig. 5. We recall that the calibration is performed by constraining the average station correction of the IV network (Italy) to zero. Some stations show a large (absolute) station corrections (e.g. stations SRO and SMOL of network SK; stations KNDS, VNDS, JAVS of network SL; station ZUGS of network BW; stations RE04 and LADO of network IV; station CT37 of network YP; station MLN of network OX). We cannot determine if the source of such large corrections are due to the metadata (as stored in EIDA) or by the state of the station. Nevertheless, even if beyond the scope of this work, such analysis also helps to identify stations that need to be checked at EIDA or by the network operators.

Stations indicated with crosses are characterized by bootstrap standard deviations larger than 0.6 m.u. and they are not further considered in this study. Finally, the spatial distribution of about 12 500 earthquakes having magnitudes with bootstrap standard deviations smaller than 0.6 are shown in Fig. 6. Note that magnitudes greater than about 6 can be affected by saturation effects due to the Wood–Anderson response. A detailed analysis of the obtained magnitudes and a comparison with existing catalogues is beyond the aim of this study which focuses on the calibration model, and it will be subject of future research.

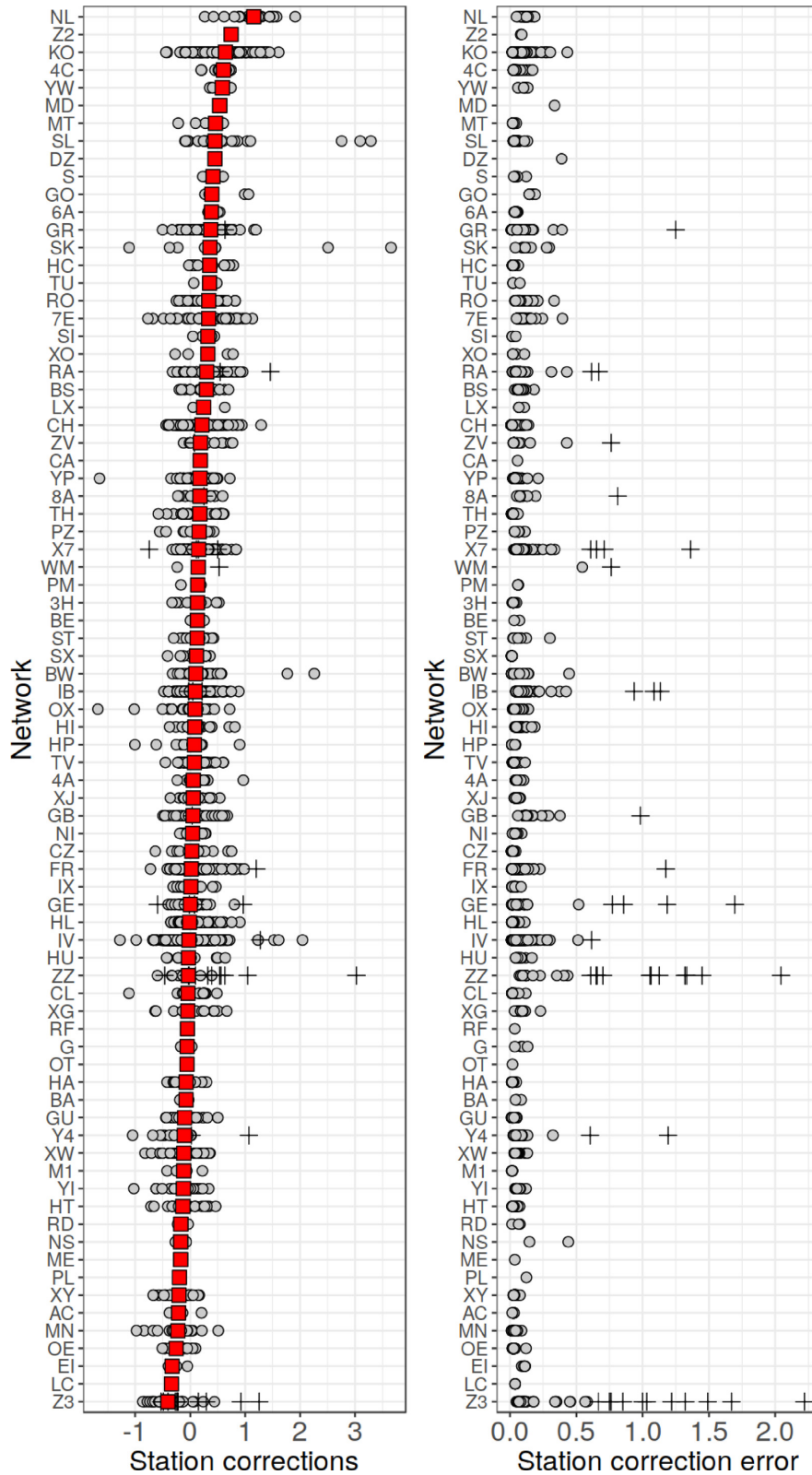


Figure 5. Non-parametric station corrections grouped by network (left-hand panel: mean bootstrap values for each station; right-hand panel: bootstrap standard deviations). Red squares indicate the mean station correction computed for each network; crosses indicate stations no further considered (bootstrap standard deviation > 0.6).

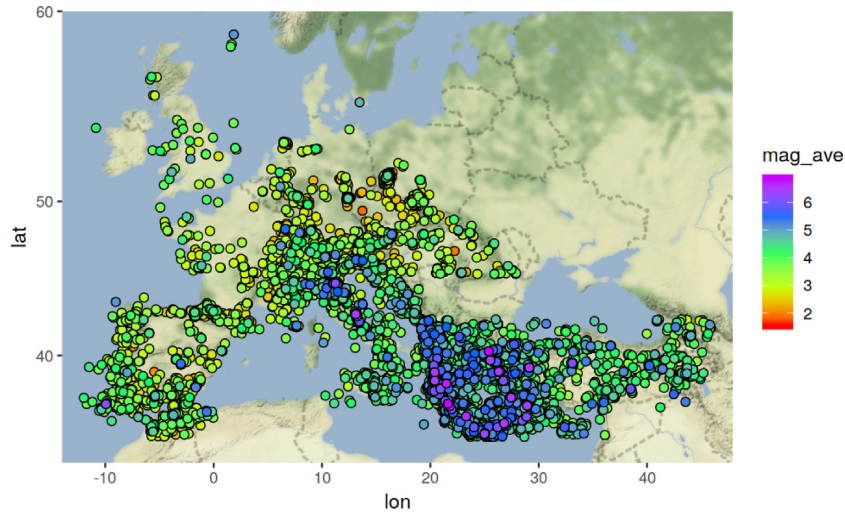


Figure 6. Location of earthquakes colour coded with the local magnitude computed following the non-parametric approach (average bootstrap solution).

4 PARAMETRIC CALIBRATION

In order to derive an attenuation model at the network level, and to evaluate the between-network variability within each region, the magnitudes calibrated through the non-parametric approach are used to develop a parametric model. The considered functional form includes two attenuation terms, one depending on the logarithm of distance and the other proportional to the distance (Hutton & Boore 1987). Using a mixed-regression approach (Pinheiro & Bates 2000; Bates *et al.* 2015), the parametric model is described by:

$$\log \tilde{A}(R) = \log A - Ml = e_1 + G(n_1, n_2, n_3; \log(R), R_a, R_b) + Q(k_1 + \Delta k_1^{net}, k_2 + \Delta k_2^{net}; R, R_a, R_b) + \delta S2S + \epsilon = \log A_0 + \delta S2S + \epsilon \quad (2)$$

In eq. (2), the logarithm of the Wood–Anderson amplitudes are corrected for the magnitude value Ml of the corresponding earthquake obtained through the non parametric approach, meaning that the parametric approach is applied only to determine the attenuation function and the station corrections. The parametric model includes an offset term (term e_1) and the so-called geometrical spreading G and anelastic attenuation Q terms. The model includes also the random effects Δk_1^{net} and Δk_2^{net} applied to k_1 and k_2 , respectively, and depending on the network, whereas $\delta S2S$ are the (magnitude) station corrections evaluated as random effects on the station grouping level. Finally, ϵ is the distribution of the event and station corrected residuals.

The geometrical spreading G is parameterized as piece-wise linear function (Atkinson & Mereu 1992; Edwards *et al.* 2008) with two breakpoints at R_a and R_b :

$$G(n_1, n_2, n_3; \log(R), R_a, R_b) = \begin{cases} n_1 \log(R) & \text{if } R \leq R_a \\ n_1 \log(R_a) + n_2 \log\left(\frac{R}{R_a}\right) & \text{if } R_a < R \leq R_b \\ n_1 \log(R_a) + n_2 \log\left(\frac{R_b}{R_a}\right) + n_3 \log\left(\frac{R}{R_b}\right) & \text{otherwise,} \end{cases} \quad (3)$$

where the slopes n_1, n_2, n_3 are considered as fixed effects. After an inspection of the data distributions and considering the results of preliminary analysis based on break-point regression (Muggeo 2003, 2008), as performed for example in Bindi *et al.* (2018), the breakpoints are fixed at 10 and 60 km in order to capture both the near source attenuation and to describe the attenuation at distances not significantly affected by the effects of secondary arrivals. It is worth noting that the distances at which Moho reflections are expected to contribute to the wavefield depend on several factors which could change from region to region such as the hypocentral depth, the crustal thickness and the impedance contrast at the Moho depth. In this study, we do not attempt to capture such regional dependency and we fix the same breakpoints for all regions. The anelastic attenuation term Q is modelled as

$$Q(k; R, R_a, R_b) = \begin{cases} 0 & \text{if } R < R_a \\ k_1(R - R_a)/100 & R_a \leq R < R_b \\ k_1(R_b - R_a)/100 + k_2(R - R_b)/100 & \text{otherwise,} \end{cases} \quad (4)$$

where the parameters k_1 and k_2 are considered as fixed effect.

4.1 Parametric results

Examples of parametric attenuation models are shown in Fig. 7, for selected national networks operating in different regions (the FDSN code of the networks are IB, RA, CH, IV and HL). Data from all networks are shown as white circles whereas those from each specific network are

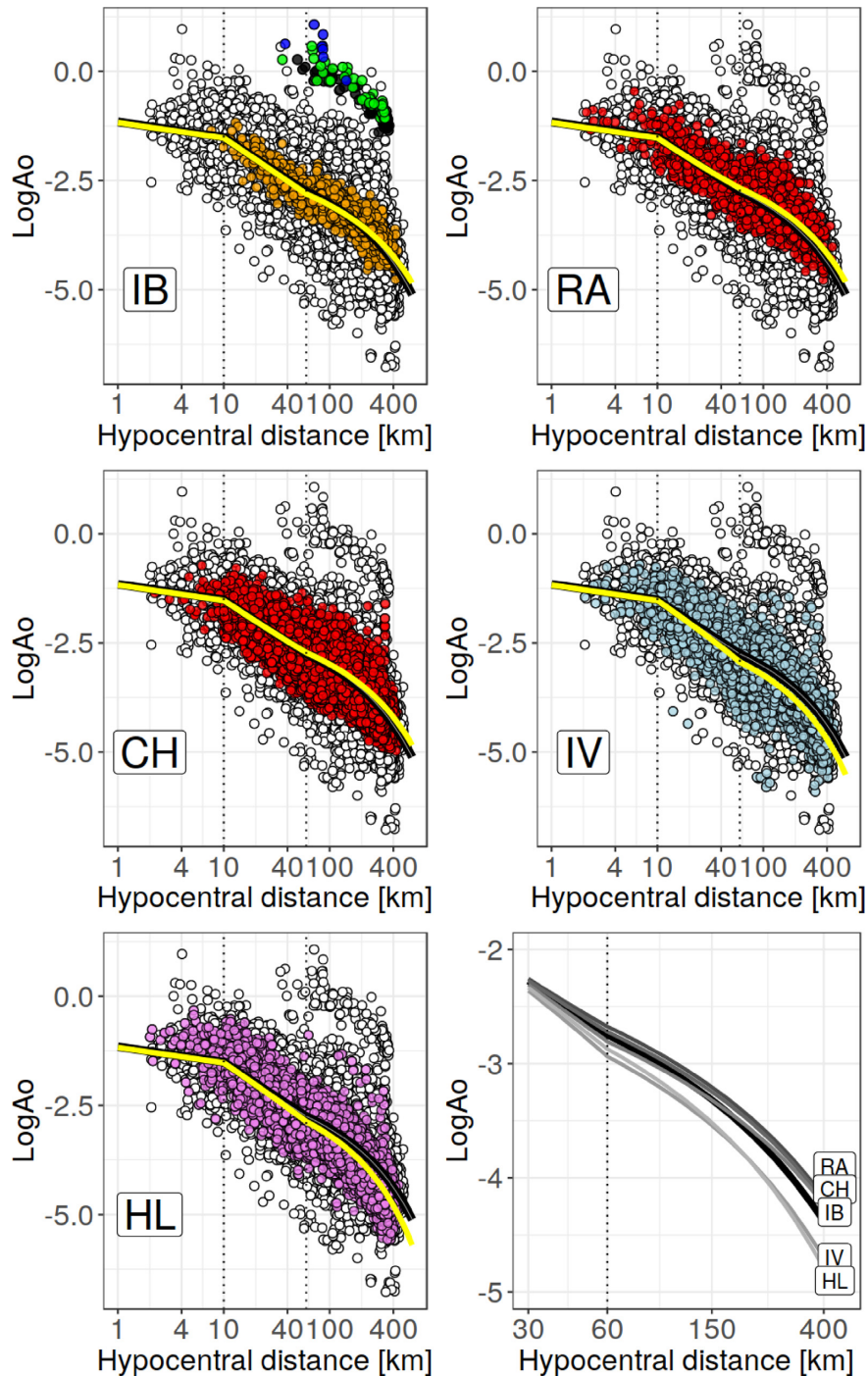
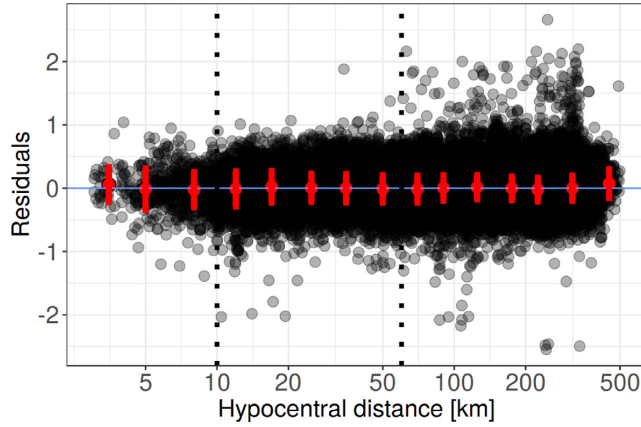


Figure 7. Parametric attenuation models $\log A_0$ obtained for five national networks (the FDSN network code is provided inside each panel). The network-dependent models are shown in yellow, the median model (i.e. without considering the network adjustments) in black. The recordings from each network are shown as circles filled according to the region mostly including the network (Fig. 2); white circles are data from other networks. In the bottom right-hand panel, the $\log A_0$ models are compared for distances above 30 km. In the panel for IB, the black, green and blue circles indicate some outliers recorded at specific stations (see text for details).

filled with the colour of the region mostly including the network (see Fig. 2). In the panel for IB, some outliers are indicated with black, green and blue circles, corresponding to station JAVS of network SL (channel HH), station KNDS of network SL (channel HH) and station SRO of network SK (channel EH), respectively. The attenuation models accounting for the network-dependent adjustments are shown in yellow whereas the model constructed considering only the fixed effects (Table 2) is shown in black. The summary reported in the bottom right frame is to highlight the presence of significant regional differences in the attenuation models. The piece-wise linear model G (eq. 3) describes a variable rate of attenuation with distance. For distances shorter than 10 km, the attenuation is weak ($n_1 = -0.353 \pm 0.038$, and strongly inverse correlated to e_1), indicating a saturation of the ground motion at short distances; in the range 10–60 km, the attenuation rate is strongest,

Table 2. Fixed effects of the parametric model (eq. 2), and entries of the covariance matrix C .

	Value	Std. error	$C_{.e_1}$	$C_{.n_1}$	$C_{.n_2}$	$C_{.n_3}$	$C_{.k_1}$
e_1	-1.157	0.037					
n_1	-0.353	0.038	-0.97				
n_2	-1.624	0.023	0.22	-0.33			
n_3	-0.750	0.010	0.03	-0.05	0.28		
k_1	0.048	0.052	-0.12	0.16	-0.55	-0.22	
k_2	-0.300	0.010	-0.01	0.01	-0.07	-0.27	0.01

**Figure 8.** Distance dependence of the residuals computed for the parametric model with breakpoints placed at 10 and 60 km (see eq. 2).

being n_2 close to -1.6 ; for longer distances, the attenuation rate decreases to about $n_3 = -0.75$. Regarding the term Q (eq. 4), its contribution is significant for $R > 60$ km, whereas it is almost zero for $R < 60$ km. The correlation between Q and G is strong over the 10–60 km distance range and decreases for larger distances ($C_{n_2, k_1} > C_{n_3, k_2}$). The network-dependent adjustments Δk_1 and Δk_2 are shown in Fig. 9. Positive values indicate less attenuation with respect to the median model constructed considering only the fixed effects. The variability among the networks is strongest for k_2 , which can be interpreted as connected to anelastic attenuation effects. Regarding k_1 , over the 10–60 km distance range, the large standard errors make Δk_1^{net} significantly different from zero only for few networks (Fig. 9). Positive Δk_2^{net} values are obtained for networks in region 1 (e.g. TH, BW, SX, GR, in Germany; CH in Swiss; RA and FR in France); among the negative values, we have HL, HT, HP in Greece, and IV (Italy). Considering large national networks, examples of positive Δk_2^{net} are $\Delta k_2^{GR} = (0.3599 \pm 0.0032)$ (German network, Region 1), $\Delta k_2^{KO} = (0.3302 \pm 0.0033)$ (Koeri network in Turkey, Region 6), $\Delta k_2^{FR} = (0.1539 \pm 0.0032)$ (France network, Region 1), $\Delta k_2^{CH} = (0.0946 \pm 0.0016)$ (Swiss network, Region 1); negative Δk_2^{net} are obtained for $\Delta k_2^{IB} = (-0.0798 \pm 0.0054)$ (Iberian network, Region 2), $\Delta k_2^{HL} = (-0.2097 \pm 0.0016)$ (Greek network, Region 6) and $\Delta k_2^{IV} = (-0.3410 \pm 0.0018)$ (Italian network, Region 3). Finally, the residuals computed for the parametric model (Fig. 8) do not show any trend with distance, even at short distances (Luckett *et al.* 2018), confirming that the breakpoints at 10 and 60 km allow to capture correctly the changes in the slope of attenuation with distance.

5 DISCUSSIONS

The availability of standardized data shared by several institutes and networks through EIDA allowed us to calibrate a harmonized local magnitude scale for central and southern Europe. The large volume of available data supported the calibration of non-parametric attenuation functions, regionalized in six geographical areas. The non-parametric approach captures the effects of the crustal heterogeneity, that result in variable rates of attenuation with distance. For example, the attenuation for region 1 (Central Europe) shows a flat trend between 60 and 120 km probably as consequence of later phase arrivals, as discussed in previous studies that highlighted the impact of Moho reflections on magnitude attenuation functions, such as those observed in Northwestern Turkey (Baumbach *et al.* 2003; Bindi *et al.* 2007) and in Northeastern Italy (Bragato & Tento 2005). Such changes in slope are difficult to capture with a parametric approach that would require the introduction of multisegment models to approximate the non-parametric curves over different distance ranges [e.g. three segments in Baumbach *et al.* (2003), and five segments in Bragato & Tento (2005)]. The results in Fig. 4 highlight significant regional differences in $\log A_0$, as quantified in Fig. 10, where the differences between the $\log A_0$ function for California (Hutton & Boore 1987) and the mean bootstrap curves are shown for all regions but region 5. Starting from the reference distance of 17 km, an attenuation stronger than in California is obtained for all regions at distances smaller than 60 km (only model 4, for the Mediterranean area, shows a similar attenuation up to 30 km). At 60 km, the trend for regions 1 and 2 (i.e. central Europe and Iberia) is reversed, as a consequence of later arrivals, leading to differences of about 0.1 m.u. at 300 km. For the Balkans (region 4), later arrivals affect the attenuation with distance starting from about 100 km, whereas for regions 4 and 6 these effects are less pronounced. Finally, regions 3, 4 and 6 show faster attenuation than California for distances larger than 150 km. Overall,

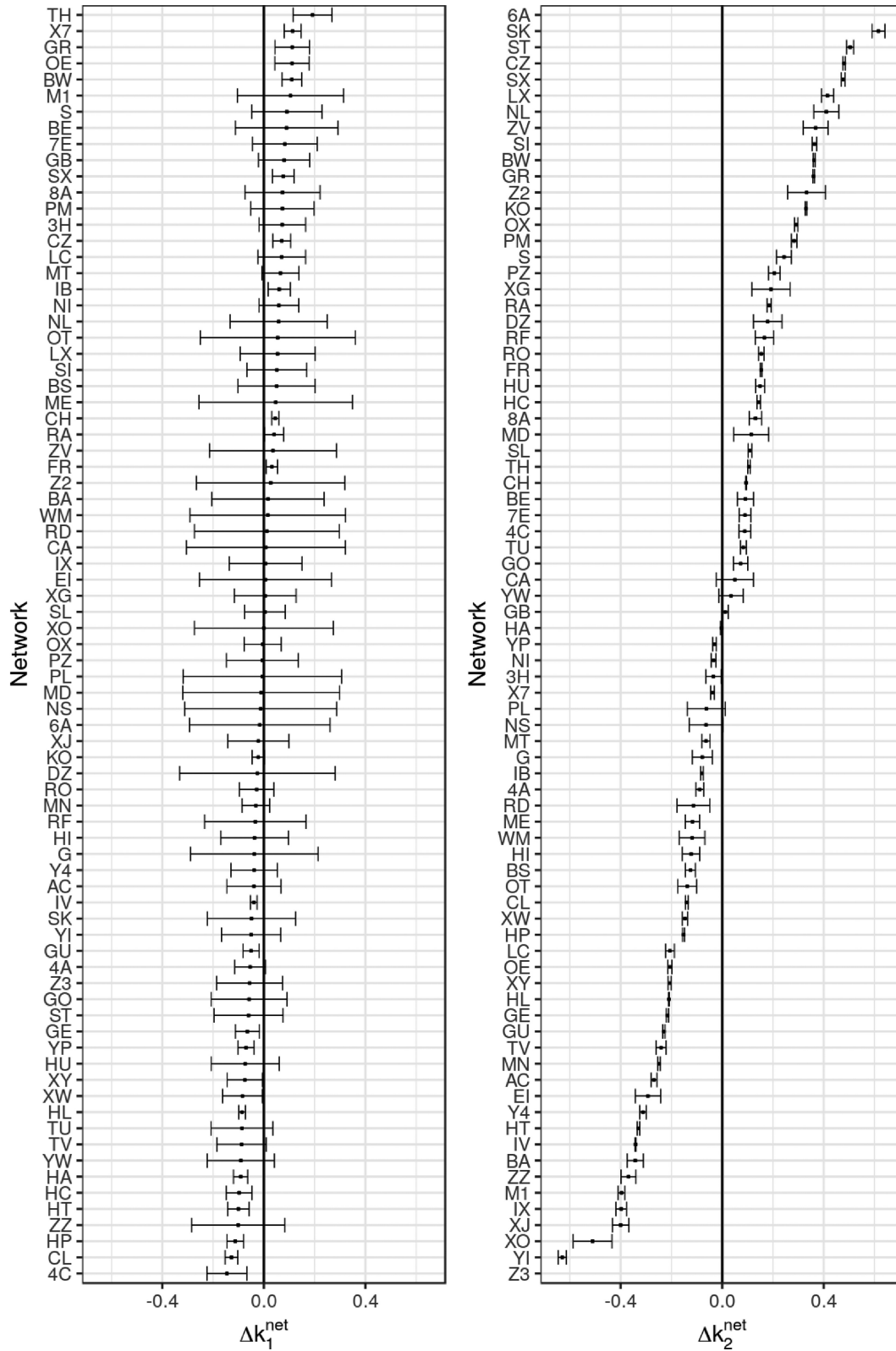


Figure 9. Network-dependent attenuation adjustments applied to k_1 (left-hand panel) and k_2 (right-hand panel) as random effects, see eq. (2).

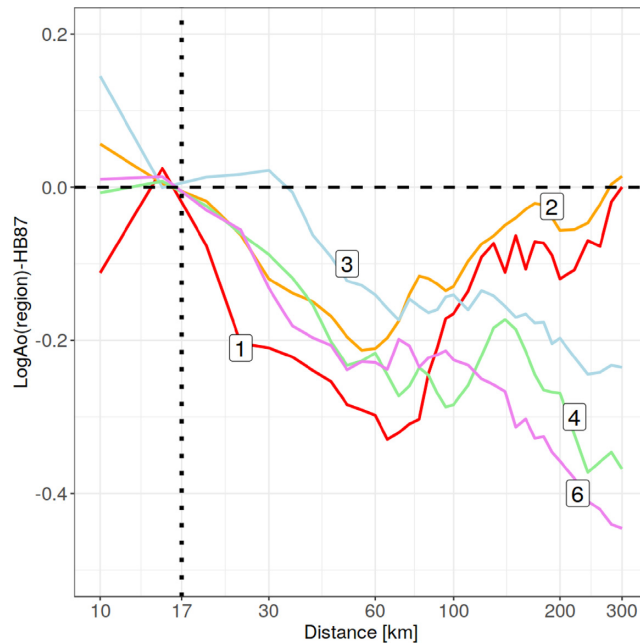


Figure 10. Difference between the non-parametric attenuation models $\log A_0$ for each region (as identified by the corresponding number) shown in Fig. 4 and the model for California (Hutton & Boore 1987).

the variability of the $\log A_0$ across the six regions is significant, in particular for distances larger than 60 km, leading to differences larger than 0.4 m.u. at 400 km.

Through the mixed effects regression, we evaluated the between-network variability of $\log A_0$ within the same region or within the same country. Fig. 11 exemplifies the case for Greece (top panels), France (middle panels) and Germany (bottom panels). For Greece, we considered the HL (National Observatory Athens), HA (University of Athens), HT (Aristotle University Thessaloniki), HP (University of Patras) and HC (Crete seismic network) networks, shown in the maps of Fig. 11. The attenuation functions show similar trends well approximating the non-parametric attenuation obtained for region 6. The difference between $\log A_0$ computed for each network with respect to $\log A_0$ for network HL [i.e. $\log A_0(\text{network}) - \log A_0(\text{HL})$] is shown in Fig. 12, top panel. The differences for HA, HP and HT are within ± 0.1 m.u., and slightly larger for HC. In particular, $\log A_0$ for HC and HA shows a slower decay than HL in the first 60 km, whereas the decay is slightly faster for HT.

For France (middle panels in Figs 11 and 12), we considered two national networks, that is the seismological FR network (RESIF) and the strong motion network RA (RAP), and the temporary network X7 (RESIF-PYROPE) operating from 2010 to 2014 in the Pyrenees area and in the western part of France. Network X7 also includes three profiles deployed across the Pyrenees for 1 yr. The $\log A_0$ functions for FR and RA are very similar, with differences within 0.05 m.u. (Fig. 12). The attenuation for X7 is stronger in the first 60 km, and weaker for larger distances with differences between -0.1 (at 60 km) and 0.18 (at 400 km). The $\log A_0$ function for X7 (Fig. 11) is similar to the non-parametric model for Region 2 (Iberia) whereas the FR and RA models show an attenuation below 60 km slightly weaker than the non-parametric solution for Region 1 (central Europe). Since networks FR and RA have been installed for different purposes, RA being oriented to engineering seismology applications, the recording sites have different characteristics. Fig. 13 (top panel), compares the magnitude stations corrections for the three networks. The larger average correction obtained for RA (0.04) than for FR (-0.15) confirms that the RA station locations are, on average, more affected by local site amplification effects.

For Germany, we considered the German national network (GR) and the regional networks BW (Bayern network), TH (Thüringer network), and SX (Saxon network). Furthermore, we added the Swiss network (CH) as term of comparison. The attenuation functions for GR and BW are almost identical over the whole distance range. For distances below 60 km, the $\log A_0$ functions for SX and TH networks show weaker and strong attenuation than GR, respectively, but the trends reverse for larger distances. Nevertheless, the curves are similar, showing differences within ± 0.15 m.u. The models obtained for the German networks are less attenuated than the non-parametric model for Region 1 which is, for distances above 100 km, very close to the parametric solution for the CH (bottom right) and FR (middle right) networks, which record several earthquakes in Italy at large distances (blue rays). Finally, the average station corrections of the German networks are negative (Fig. 13).

6 CONCLUSION

We took advantage of the European Integrated Data Archive (EIDA) to develop the first harmonized local magnitude scale for central and southern Europe. The possibility to refer to a harmonized magnitude scale, and to run non-parametric calibrations, allowed us to highlight

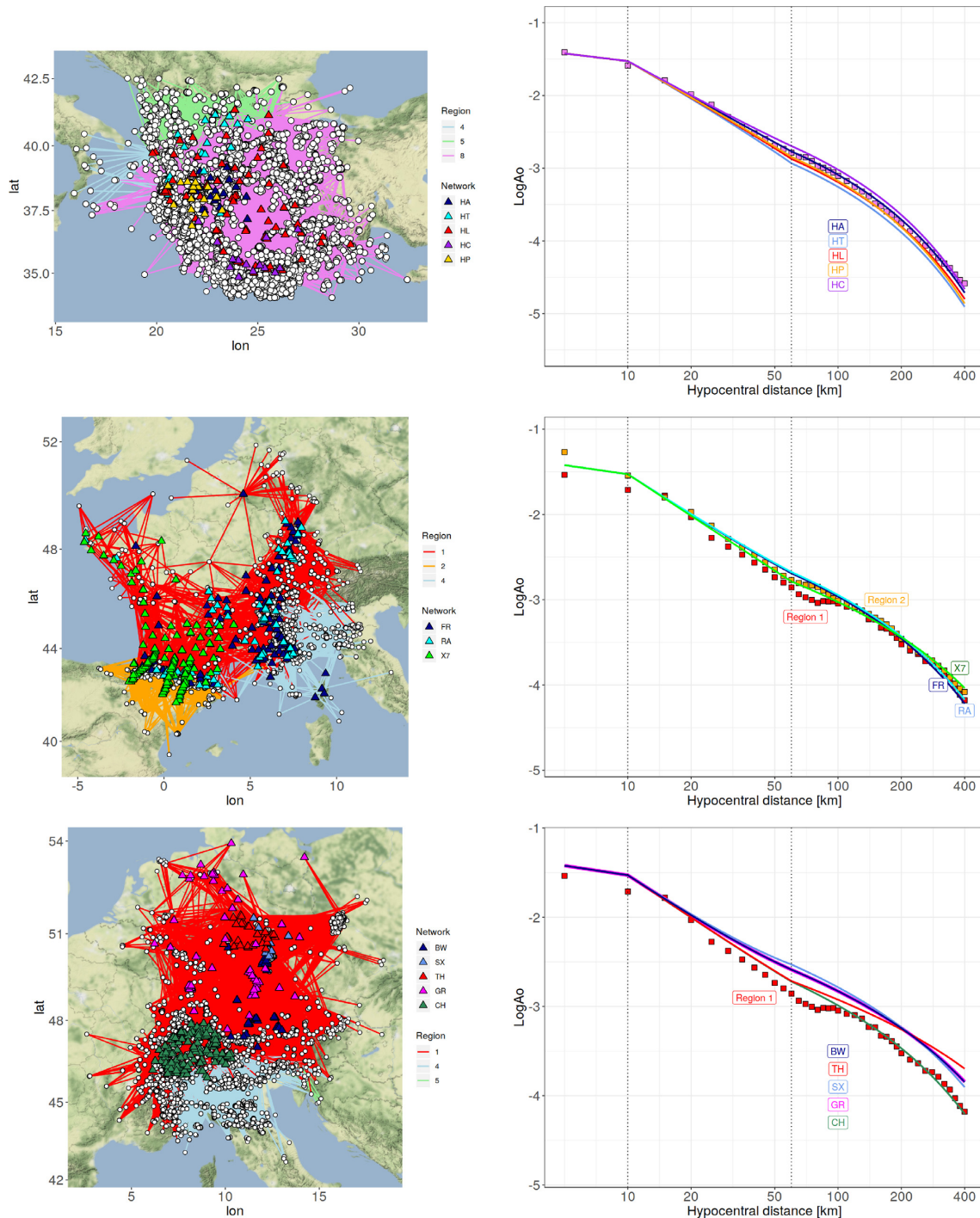


Figure 11. Parametric results for Greece (top), France (middle), and Germany (bottom). In the results for Germany, the Swiss network CH is also considered as term of comparison. The maps on the left show: the station locations (triangles) colour coded with the network; the epicenters of recorded earthquakes (circles); the ray paths colour coded according to which region each path is contributing (see Fig. 2). In the right plots, squares indicate the non-parametric $\log A_0$ models for region 1 (red) and 2 (orange), while the parametric models for each network is colour coded according to the network as in the maps. The FDSN network codes are also given in each plot. The vertical dotted lines indicate the hinge distances of the parametric models.

and quantify regional differences in the attenuation models, both in terms of overall attenuation differences and in terms of changes of the attenuation rate with distance related to crustal heterogeneity (e.g. effects of later arrivals). The main conclusions are the following:

- (i) the non-parametric analysis shows that $\log A_0$ has strong regional characteristics within the study area and the rate of attenuation changes significantly over different distance ranges;
- (ii) the non-parametric analysis shows that the attenuation for distances smaller than 60 km is stronger than the attenuation predicted by the model for California (Hutton & Boore 1987), causing differences up to 0.3 m.u. at 60 km; for larger distances, $\log A_0$ differences exceeding

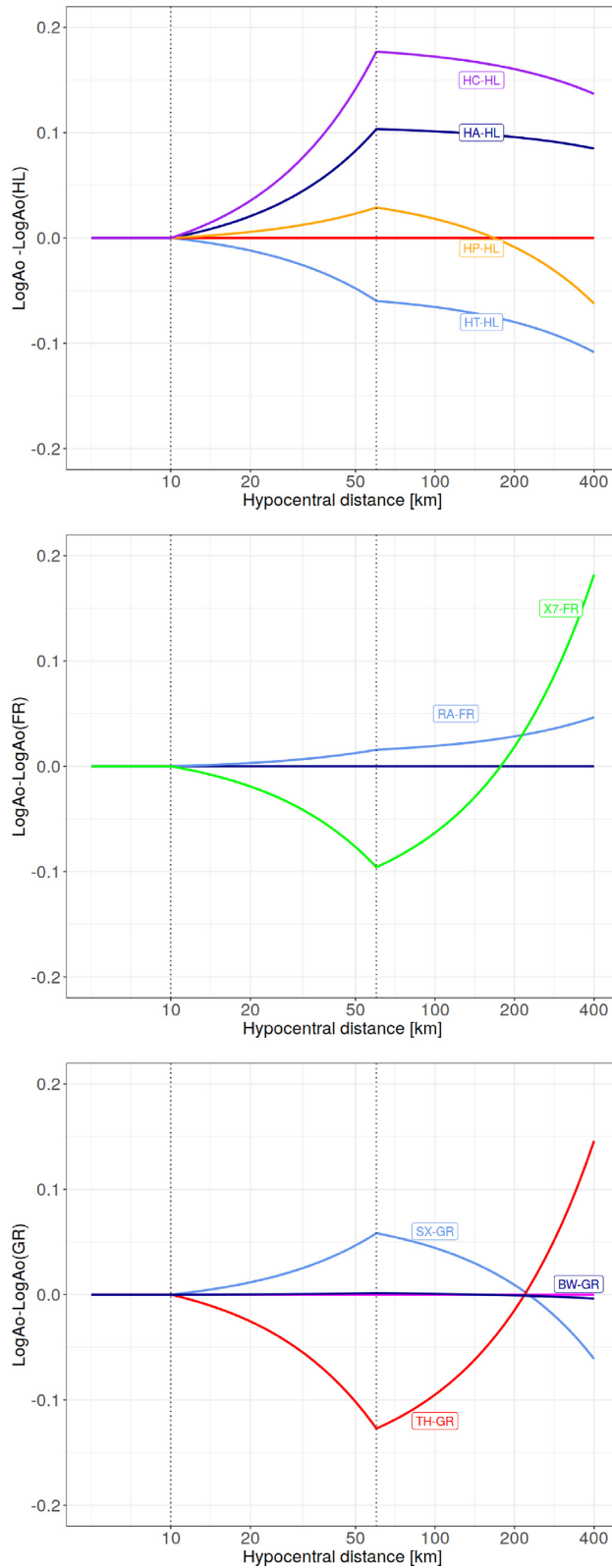


Figure 12. Difference among the parametric attenuation functions for networks in Greece (top), France (middle), Germany (bottom), see also Fig. 11.

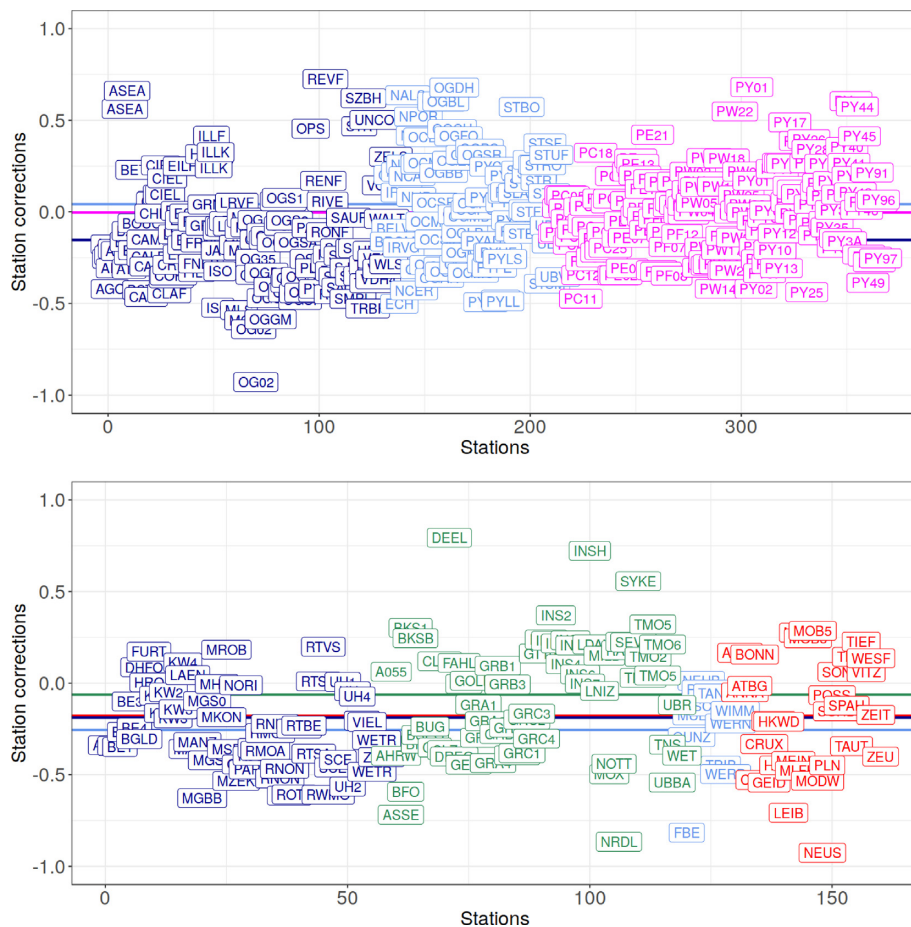


Figure 13. Station corrections δS_2S (see eq. 2) for selected networks in France (top) and Germany (bottom). The average corrections for each network (identified by different colours) are shown as horizontal lines.

0.4 m.u. at 400 km are observed among regions in central and southern Europe; moreover, later arrivals have a strong influence on $\log A_0$ at distances between 60 and 120 km;

(iii) considering national seismic networks, the network-dependent adjustments $\Delta k_2^{network}$ applied to the parametric models are negative (stronger attenuation than the median model for distances larger than 60 km) for HL (Greece) and IV (Italy), positive (weaker attenuation) for KO (Turkey), GR (Germany), FR (France) and CH (Swiss); for several countries, the between-network variability among $\log A_0$ functions for networks operating in the same country is within ± 0.2 m.u.

In conclusion, the availability of a harmonized magnitude scale makes easier the operation of comparing and merging catalogues provided by different networks and allows to jointly analyse amplitudes recorded at stations belonging to different networks operating in adjacent regions. Future work will look into the ISC Bulletin and comparison between the M_I obtained from the homogenized calibration functions here presented and the reported M_I to the ISC.

7 DATA AND RESOURCES

In this study, we used data and information downloaded from the following sites: EIDA (<https://www.orfeus-eu.org/data/eida/>); EMSC (<http://seismicportal.eu/fdsn/event/1/query>); FDSN (<https://www.fdsn.org/networks/>). The derivation of the models was performed using R software (R Core Team 2018) and, in particular, lme4 (Bates et al. 2015), dplyr (Wickham et al. 2018), ggplot2 (Wickham 2016), ggmap (Kahle & Wickham 2013), sf (Pebesma 2018), Segmented (Muggeo 2008) and sparseM (Koenker & Ng 2017) packages. For information about stream2segment package, see (Zaccarelli 2018). Tables listing attenuation coefficients and station corrections derived in this study are available in Bindi et al. (2019b).

ACKNOWLEDGEMENTS

We thank the networks operators for providing data and metadata used in this study through EIDA, EMSC and ISC. This work has been partially funded by the European H2020 project Seismology and Earthquake Engineering Research Infrastructure Alliance for Europe (SERA,

<http://www.sera-eu.org>) and by EPOS-IP project (European Union's Horizon 2020 research and innovation program under grant agreement N° 676564). We thank two anonymous Reviewers and Martin Mai for their helpful comments.

REFERENCES

- Alsaker, A., Kvamme, L.B., Hansen, R.A., Dahle, A. & Bungum, H., 1991. The M_L scale in Norway, *Bull. seism. Soc. Am.*, **81**, 379–398.
- Al Atik, L., Abrahamson, N., Bommer, J.J., Scherbaum, F., Cotton, F. & Kuehn, N., 2010. The variability of ground-motion prediction models and its components, *Seimol. Res. Lett.*, **81**(5), 794–801.
- Atkinson, G.M. & Mereu, R., 1992. The shape of ground motion attenuation curves in southeastern Canada, *Bull. seism. Soc. Am.*, **82**, 2014–2031.
- Bates, D., Mächler, M., Bolker, B. & Walker, S., 2015. Fitting linear mixed-effects models using lme4, *J. Stat. Software.*, **67**, 1–48.
- Baumbach, M. *et al.*, 2003. Calibration of an M_L scale in Northwestern Turkey from 1999 Izmit aftershocks, *Bull. seism. Soc. Am.*, **93**, 2289–2295.
- Bindi, D., Parolai, S., Görgün, E., Grosser, H., Milkereit, C., Bohnhoff, M. & Durukal, E., 2007. M_L scale in Northwestern Turkey from 1999 Izmit aftershocks: updates, *Bull. seism. Soc. Am.*, **97**, 331–338.
- Bindi, D., Massa, M., Luzi, L., Ameri, G., Pacor, F., Puglia, R. & Augliera, P., 2014. Pan-European ground-motion prediction equations for the average horizontal component of PGA, PGV, and 5 per cent-damped PSA at spectral periods up to 3.0 s using the RESORCE dataset, *Bull. Earthq. Eng.*, **12**, 391–430.
- Bindi, D., Cotton, F., Kotha, S.R., Bosse, C., Stromeyer, D. & Grünthal, G., 2017. Application-driven ground motion prediction equation for seismic hazard assessments in non-cratonic moderate-seismicity areas, *J. Seismol.*, **21** (5), 1201–1218.
- Bindi, D., Spallarossa, D., Picozzi, M., Scafidi, D. & Cotton, F., 2018. Impact of magnitude selection on aleatory variability associated with Ground-Motion Prediction Equations: Part I—local, energy, and moment magnitude calibration and stress-drop variability in central Italy, *Bull. seism. Soc. Am.*, **108**(3A), 1427–1441.
- Bindi, D., Picozzi, M., Spallarossa, D., Cotton, F. & Kotha, S.R., 2019a. Impact of magnitude selection on aleatory variability associated with Ground Motion Prediction Equations: Part II—analysis of the between-event distribution in central Italy, *Bull. seism. Soc. Am.*, **109**(1), doi:10.1785/0120180239.
- Bindi, D., Zaccarelli, R., Strollo, A. & Di Giacomo, D., 2019b. Attenuation coefficients and station corrections for harmonized local magnitude scales in Europe. V. 1.0. GFZ Data Services, doi:10.5880/GFZ.2.4.2019.003.
- Booth, D., 2007. An improved UK local magnitude scale from analysis of shear and Lg-wave amplitudes, *Geophys. J. Int.*, **169**, 593–601.
- Bragato, P.L. & Tonto, A., 2005. Local magnitude in Northeastern Italy, *Bull. seism. Soc. Am.*, **95**, 579–591.
- Cauzzi, C., Sleeman, R., Clinton, J., Ballesta, J.D., Galanis, O. & Kästli, P., 2016. Introducing the European Rapid Raw Strong-Motion database, *Seim. Res. Lett.*, **87**, 977–986.
- Chovanová, Z. & Kristek, J., 2018. A local magnitude scale for Slovakia, Central Europe, *Bull. seism. Soc. Am.*, **108** (5A), 2756–2763.
- Converse, A.M. & Brady, A.G., 1992. BAP: Basic strong-motion accelerometer processing software, version 1.0, U.S. Geol. Surv. Open-File Rept. 92-296A, 174pp.
- Deichmann, N., 2017. Theoretical basis for the observed break in M_L/M_w scaling between small and large earthquakes, *Bull. seism. Soc. Am.*, **107** (2), 505–520, .
- Deichmann, N., 2018. Why does M_L scale 1:1 with $0.5 \log E_s$? *Seimol. Res. Lett.*, **89**, 2249–2255.
- Di Bona, M., 2016. A local magnitude scale for crustal earthquakes in Italy, *Bull. seism. Soc. Am.*, **106**, 242–258.
- Edwards, B., Rietbrock, A., Bommer, J.J. & Baptie, B., 2008. The acquisition of source, path, and site effects from microearthquake recordings using Q tomography: application to the United Kingdom, *Bull. seism. Soc. Am.*, **98**, 1915–1935.
- Efron, B., 1979. Bootstrap methods, another look at the jackknife, *Ann. Stat.*, **7**, 1–26.
- Grünthal, G. & Wahlström, R., 2012. The European-Mediterranean Earthquake Catalogue (EMEC) for the last millennium, *J. Seismol.*, **16**, 535–570.
- Hutton, L.K. & Boore, D.M., 1987. The M_L scale in Southern California, *Bull. seism. Soc. Am.*, **77**, 2074–2094.
- Kahle, D. & Wickham, H., 2013. ggmap: spatial visualization with ggplot2, *R Journal*, **5**, 144–161.
- Kanamori, H., Hauksson, E., Hutton, L.K. & Jones, L.M., 1993. Determination of earthquake energy release and M_L using TERRASCOPE, *Bull. seism. Soc. Am.*, **83**, 330–346.
- Kiliç, T., Ottemöller, L., Havskov, J., Yanik, K., Kiliçarslan, Ö., Alver, F. & Özyazicioğlu, M., 2017. Local magnitude scale for earthquakes in Turkey, *J. Seismol.*, **21** (1), 35–46.
- Koenker, R. & Ng, P., 2017. SparseM: Sparse Linear Algebra, R package version 1.77, Available at <https://CRAN.R-project.org/package=SparseM>.
- Kotha, S.R., Bindi, D. & Cotton, F., 2017. From ergodic to region- and site-specific probabilistic seismic hazard assessment: method development and application at European and Middle Eastern sites, *Earthq. Spectra*, **33**, 1433–1453.
- Luckett, R., Ottemöller, L., Butcher, A. & Baptie, B., 2018. Extending local magnitude M_L to short distances, *Geophys. J. Int.*, **216**, 1145–1156.
- Muggeo, V.M.R., 2003. Estimating regression models with unknown breakpoints, *Stat. Med.*, **22**, 3055–3071.
- Muggeo, V.M.R., 2008. Segmented: an R package to fit regression models with broken-line relationships, *R News*, Vol. **8/1**, 20–25, Available at <https://cran.r-project.org/doc/Rnews/> (last accessed November 2017).
- Pebesma, E., 2018. sf: Simple features for R, R package version 0.6-3, <https://CRAN.R-project.org/package=sf>.
- Pinheiro, J.C. & Bates, D.M., 2000. *Mixed-Effects Models in S and S-Plus*, Springer-Verlag, pp. 57–96.
- R Core Team, 2018. *R: A language and environment for statistical computing, R Foundation for Statistical Computing*, Vienna, Austria, Available at <https://www.r-project.org/>, (last accessed June 2018).
- Richter, C., 1935. An instrumental earthquake magnitude scale, *Bull. seism. Soc. Am.*, **25**, 1–32.
- Savage, M.K. & Anderson, J.G., 1995. A local-magnitude scale for the western great basin-eastern Sierra Nevada from synthetic Wood-Anderson seismograms, *Bull. seism. Soc. Am.*, **85**, 1236–1243.
- Scordilis, E.M., Kementzidou, D. & Papazachos, B.C. 2016. Local magnitude calibration of the Hellenic unified seismic network, *J. Seismol.*, **20**, 319–332.
- Spallarossa, D., Bindi, D., Augliera, P. & Cattaneo, M., 2002. An M_L scale in northwestern Italy, *Bull. seism. Soc. Am.*, **92**, 2205–2216.
- Stange, S., 2006. M_L determination for local and regional events using sparse network in Southwestern Germany, *J. Seismol.*, **10**, 247–257.
- Uhrhammer, R.A. & Collins, E.R., 1990. Synthesis of Wood-Anderson seismograms from broadband digital records, *Bull. seism. Soc. Am.*, **80**, 702–716.
- Wickham, H., 2016. *ggplot2: Elegant Graphics for Data Analysis*, Springer-Verlag, isbn:978-3-319-24277-4
- Wickham, H., François, R., Henry, L. & Müller, K., 2018. dplyr: A Grammar of Data Manipulation. R package version 0.7.6. <https://CRAN.R-project.org/package=dplyr>.
- Zaccarelli, R., 2018. Stream2segment: a tool to download, process and visualize event-based seismic waveform data. v. 2.7.3. GFZ Data Services, doi:10.5880/GFZ.2.4.2019.002.
- Zaccarelli, R., Bindi, D., Strollo, A., Quinteros, J. & Cotton, F., 2019. Stream2segment: an open source tool for downloading, processing and visualizing massive event-based seismic waveform datasets, *Seimol. Res. Lett.*, submitted.